

Article

Generating 3D Geothermal Maps in Catalonia, Spain Using a Hybrid Adaptive Multitask Deep Learning Procedure

Seyed Poorya Mirfallah Lialestani ^{1,*} , David Parcerisa ¹ , Mahjoub Himi ² and Abbas Abbaszadeh Shahri ³ 

- ¹ Department of Mining, Industrial and ICT Engineering, Universitat Politècnica de Catalunya, Av. Bases de Manresa 61-73, 08242 Manresa, Spain; david.parcerisa@upc.edu
- ² Department of Mineralogy, Petrology and Applied Geology, University of Barcelona, 08007 Barcelona, Spain; himi@ub.edu
- ³ Johan Lundberg AB, 754 50 Uppsala, Sweden; shahri.abbas@bircham.edu
- * Correspondence: poorya.mirfallah@upc.edu

Abstract: Mapping the subsurface temperatures can efficiently lead to identifying the geothermal distribution heat flow and potential hot spots at different depths. In this paper, an advanced adaptive multitask deep learning procedure for 3D spatial mapping of the subsurface temperature was proposed. As a result, predictive 3D spatial subsurface temperatures at different depths were successfully generated using geolocation of 494 exploratory boreholes data in Catalonia (Spain). To increase the accuracy of the achieved results, hybridization with a new modified firefly algorithm was carried out. Subsequently, uncertainty analysis using a novel automated ensemble deep learning approach for the predicted temperatures and generated spatial 3D maps were executed. Comparing the accuracy performances in terms of correct classification rate (CCR) and the area under the precision–recall curves for validation and whole datasets with at least 4.93% and 2.76% improvement indicated for superiority of the hybridized model. According to the results, the efficiency of the proposed hybrid multitask deep learning in 3D geothermal characterization to enhance the understanding and predictability of subsurface spatial distribution of temperatures is inferred. This implies that the applicability and cost effectiveness of the adaptive procedure in producing 3D high resolution depth dependent temperatures can lead to locate prospective geothermally hotspot active regions.

Keywords: 3D spatial subsurface temperature; geothermal energy; Catalonia; hybrid adaptive multitask deep learning; predictive model



Citation: Mirfallah Lialestani, S.P.; Parcerisa, D.; Himi, M.; Abbaszadeh Shahri, A. Generating 3D Geothermal Maps in Catalonia, Spain Using a Hybrid Adaptive Multitask Deep Learning Procedure. *Energies* **2022**, *15*, 4602. <https://doi.org/10.3390/en15134602>

Academic Editor: Dameng Liu

Received: 25 May 2022

Accepted: 20 June 2022

Published: 23 June 2022

Publisher's Note: MDPI stays neutral with regard to jurisdictional claims in published maps and institutional affiliations.



Copyright: © 2022 by the authors. Licensee MDPI, Basel, Switzerland. This article is an open access article distributed under the terms and conditions of the Creative Commons Attribution (CC BY) license (<https://creativecommons.org/licenses/by/4.0/>).

1. Introduction

Access to energy resources is a critical worldwide issue. From this point of view, renewable power is emerging as an innovative cost-effective and clean source of energy for the future. Accordingly, the renewable resources are increasingly displacing fossil fuels in the power sector because of their capability to reduce carbon emissions and other types of pollution. However, several marketed renewable resources (e.g., biomass and large hydroelectric dams) due to some problematic tradeoffs may not be suitable to the geoenvironmental concerns [1]. In the field of renewables, geothermal is always available to be tapped and thus in comparison with other resources provides a reliable source of power [2]. Moreover, the low carbon intensity than the solar photovoltaic makes it a useful tool against the advance of climate change. Furthermore, versatility of geothermal resources dedicates particularly useful for promoting economic diversification [3,4].

The view of the increasing trend of the consumed energy in Europe and subsequently worldwide dependency on the external sources attractively moves toward developing the use of renewable energies and, in particular, geothermal resources as an appropriate solution [5,6]. Referring to Chamorro et al., (2014) [7], Spain can significantly be benefited from the high capacity of the natural geothermal resources. This is because in the Iberian Peninsula, the temperature can reach high values at shallow depths. Accordingly, in recent

years using shallow geothermal resources have depicted steady growth and popularity in the construction subsector, whereas in power generation due to associated problem with electricity, unequal progress was reported [8,9].

The temperature of geothermal resources originating from the continuously produced heat within the earth can be classified into high ($T > 225\text{ }^{\circ}\text{C}$), intermediated ($125\text{--}225\text{ }^{\circ}\text{C}$), and low ($T < 125\text{ }^{\circ}\text{C}$) systems [10]. To achieve this source of energy, the knowledge on subsurface geological hot spots for more precise drilling to access the target temperature is of great importance [11]. Therefore, to assess the well productivity, several parameters such as morphology and temperature of the ground, geothermal gradient, porosity, permeability, fluid salinity, thermal conductivity, and specific heat capacity at various depths play a critical role [12]. However, all this information often is not accessible [13] and also continuous or periodically monitoring the equipped test boreholes with temperature sensors is a time-consuming and costly procedure [4]. This is the reason why the geoengineering characteristics depend on the scale of the project are often approximated with different techniques and computer modelling approaches [14–17]. Producing 3D conceptual shallow geothermal potentials [18,19], utilizing GIS [20–22], spatial data analysis [23–25], applying numerical technique [26–29], integrated of different geophysical prospecting techniques such as magnetotelluric [30–34], gravity [33,35], seismic [31,33], and electrical resistivity [31,36,37], as well as evident geological characteristics [38,39] are some of the carried efforts in Spain, Chile, Pakistan, Iran, India, Nigeria, Indonesia, Denmark, China, Thailand, Italy, Taiwan, Finland and Japan. However, simulating the geothermal resources using numerical techniques due to complexity of the model preparation (natural state properties of the rocks and geothermal system), description of the realistic problem and evaluation of the results as well as inability in providing any insight into generalizations is a very time-consuming task that demands extensive experience. In case of GIS, learning curve can be long where the spatial relationships do not lead to absolute solutions and also the integration with traditional map is difficult [40–42]. Such drawbacks in generating high resolution 3D maps due to dedicating more flexibility but higher computational and analytical capabilities can be handled by artificial intelligence (AI) approaches. The skilled AI-based models in geoengineering problems were used to tackle the difficulties in handling the big data [43] and provide physically meaningful relationships within geo-data [44–46]. Accordingly, applicability of the AI techniques in the form of artificial neural network, machine/deep learning, evolutionary algorithms, and hybrid structures in producing the predictive 3D subsurface models have been highlighted [46–51]. Due to characterized features in creating transferable solutions and learnability from high-level data attributes [52] the feasibility of AI techniques in geothermal modeling [53,54] and compared performance by field prospecting methods [55,56] have been notified in several studies dealing with predicting the location of hot spot structures [57–60], estimating the temperature distribution [61,62], and potential of geothermal production associated with geological data [63,64].

Referring to literature reviews, the AI models can be optimized through metaheuristic algorithms to find the most proper solutions relative to a set of prioritized criteria or constraints [65–68]. However, the optimizing performance of these algorithms due to analytical shortcomings cannot be guaranteed [65,69]. This limitation of metaheuristic algorithms with growing interested in optimization methods can be covered using modification process to improve the performance and prevent from computational costs of a rework [69–71].

The firefly algorithm (FA) [72] is a developed swarm optimization method based on the attractiveness of fireflies, but suffers from slow convergence and getting trapped in local optimum for multimodal problems [73]. In this paper a new developed version of modified FA by Abbaszadeh Shahri et al., 2022a [69] is used.

In this point of view, Spain, despite the access to high potential of different types of geothermal resources is still far from achieving a generalized utilizing of these renewable systems [74]. However, following the European initiatives, based on the 2011–2020 renewable energy plan, Spain is also working on promising geothermal areas for both power production and direct applications [75]. Due to the lack of worldwide characterized information of subsurface geothermal hotspots [8], developing the modelling techniques for evaluation, and utilizing these resources critically should be considered as one of the most prolific tasks for contributing to the global sustainability [18,76–78]. Moreover, the information of subsurface soils often is acquired from the vertical sparse exploratory boreholes in which laterally spatial distribution of predicted parameter is a difficult task [46,47,49]. This implies that evaluating the models aiming to identify the possible hotspots can lead to utilize and decrease the available gaps of this resource with respect to other European nations and would allow Spain to reduce its foreign energy dependency. Such demands crucially motive for developing new computational modelling techniques leading to new frameworks for the future expansion of this energy.

Despite the demonstrated more precise results in hybridized AI techniques with the high-level metaheuristic optimization algorithms [69], no distinguished work dealing on developing multi-task predictive models through platform of intelligence systems in geothermal application is available. Multi-task learning is inherently a multi-objective problem because different tasks may conflict, necessitating a trade-off [79] and thus has received considerable attention in real-world problems. In such learning schemes multiple tasks are solved jointly and sharing inductive bias between tasks. Therefore, referring to the above-mentioned concerns and the progressively emerged interest in developing 3D digital models, an adaptive hybridized multi-task deep learning AI procedure for generating spatial subsurface temperature at different depths in Catalonia, Spain, was developed. Hybridizing process was carried out through a new version of modified firefly algorithm (MFA). The modelling procedure was executed through 496 numbers of sparse data comprising latitude, longitude, elevation, and surface temperature. Accordingly, the temperatures at depths 50 and 150 m were predicted, and the model then was setup to provide estimation for 120 and 180 m, respectively. The evaluated receiver operating characteristic (ROC) supplemented by error analysis showed the applicability and cost effectiveness of the adopted multitask procedure in producing high resolution depth dependent subsurface temperature maps for the study area. Subsequently, an uncertainty analysis using an introduced state-of-the-art approach for the predicted temperature and generated spatial maps were conducted.

2. Materials and Methods

2.1. Study Area and Acquired Datasets

Catalonia is a province of Spain located at the north-east of the Iberian Peninsula, in the western Mediterranean area with a diverse range of geomorphological features from mountainous to coastal landscapes [80,81]. This study is focused in an area of 7942 km² in the northeastern part of Catalonia, as presented in Figure 1. The northern domain is a mountainous territory corresponding to the eastern part of the Pyrenees and the southern limb tie in with the Catalan Coastal Ranges that are parallel to the Mediterranean shoreline. The area is made up by a Paleozoic continental crust affected by extensive sedimentary basins during Mesozoic and Neogene and a compressive basin of Paleogene age coeval with the development of the Pyrenees and the Catalan Coastal Ranges [82,83].

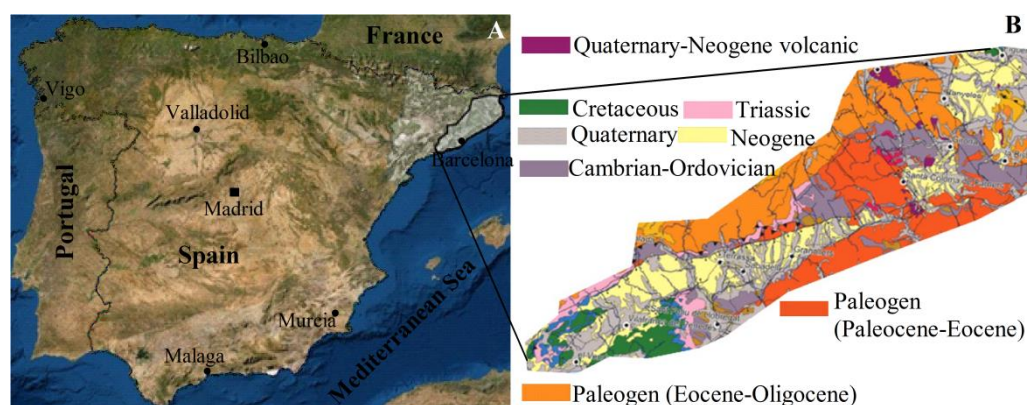


Figure 1. The location of study area in Spain (A) and the corresponding geological settings (B).

Previous carried out research implied on ideal geothermal inquiry in several regions of this area such as Vallès, Empordà, La Selva, Penedès, Fossa d’Olot, Plana de Vic, Depressió Central (Lleida), and Maresme. Accordingly, in this study, a number of 496 stochastic datasets including longitude (X), latitude (Y), elevation (Z) and surface temperature (T_s) were derived from the database of the Catalonia Cartographic and Geological Institute (ICGC) [84,85]. The used database in the current paper was constructed from the compiled annually time-dependent information provided by ICGC for the year of 2021 at each measuring station or control point. The acquired datasets for further procedure were randomized and split into 65%, 20% and 15% to establish the training, testing, and validation sets and after compiling were normalized within $[0, 1]$ interval to increase the learning speed and model stability.

2.2. Deep Neural Learning Structure

Multitask learning can increase the generalization of deep neural learning structures (DNLS) by employing domain information contained in the training inputs of related tasks as an inductive bias. In comparison to training the models independently, this learning procedure aims to tackle multiple tasks at the same time to enhance efficiency and prediction accuracy [79,86]. This implies on performing parallel learning with a shared representation, in which each task can help other tasks be learned better [87–89].

As shown in Figure 2, DNLS is a subcategory of AI techniques with multiple layers in which without being explicitly can scan the data to search combinable features for faster learning. This ability indicates for ameliorate feature extraction over machine learning and thus supreme performance of DNLS with unstructured data (e.g., texts, pictures, pdf, etc.) as well as exploring new complex attributes that humans might miss [90].

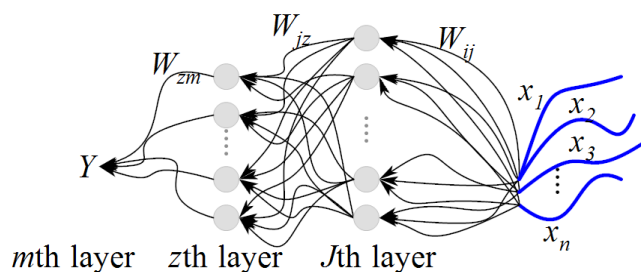


Figure 2. The topology of DNLS (the used parameters are described in the text).

In this structure, the received input signals (x_1, x_2, \dots, x_n) are passed to the hidden layers and then to the next senior level using adopted weights (w_{ij}, w_{jk}) :

$$\underbrace{x_1, \dots, x_n}_{\text{Input}} \xrightarrow{w_{ij}} \underbrace{}_{\text{Hidden layers}} \xrightarrow{w_{jk}} \underbrace{Y}_{\text{Output}} \quad (1)$$

Referring to Figure 2, the output of the j th neuron in the z th hidden layer at the t th iteration, $o_j^z(t)$, subjected to activation function, f_j^z , is defined as:

$$o_j^z(t) = f_j^z \left(\sum_{i=1}^{n_z-1} w_{ij}^z x_i^{z-1}(t) + b_j^z \right) \quad (j \leq n_z) \quad (2)$$

where n_z shows the number of neurons in the z th layer, and b_j^z denotes the bias which shifts the summed signals received from the neuron.

The outcome of the l th neuron in the m th output layer after t iteration $(Y_l(t))$, is then calculated using the updated weight by:

$$Y_l(t) = \sum_{i=1}^{n_m-1} w_{il}^m x_i^{m-1}(t) \quad (l \leq n_o) \quad (3)$$

where n_o represents the number of neurons in the output layer.

Accordingly, the error of model for entire network $(E(t))$ and predicted values $(e(t))$ are expressed as:

$$E(t) = \frac{1}{2} \sum_{j=1}^n (d_j(t) - o_j^k(t))^2 \quad (4)$$

$$e(t) = y - Y(t) \quad (5)$$

where $d_j(t)$ denotes the desired output of neuron j at the t th iteration and y shows the actual output.

In each iteration, then the weights are updated through the learning rate to minimize the prediction error of using:

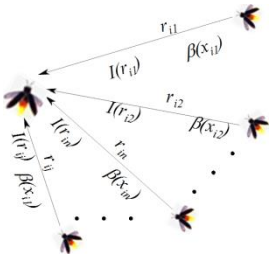
$$\Delta w(t) = -\eta_w \left(\frac{\partial E(t)}{\partial w_{old}} \right) \quad (6)$$

where η_w represent the learning rate.

2.3. The Used Modified FA (MFA)

The original FA [72] has been formulated using the attractiveness of fireflies, their brightness and adjacent distance. Table 1 shows the involved parameters in FA that depending on the problem should properly be tuned through trial-error procedure.

Table 1. Required parameters to tune the FA.

	Description	Parameter	Advised Ranges	Notation
	brightness	I	-	objective function
	attractiveness	β	-	-
	distance between two fireflies i, j	r_{ij}	-	-
	absorption coefficient	γ	[0.1–10]	-
	trade off constant in randomized movement	α	[0, 1]	randomization parameter
	attractiveness at distance 0 ($r_{ij} = 0$)	β_0	normally 1	-
	number of generations	Gen	-	iteration
	problem dimension	D	-	dimension
	number of fireflies	n	-	population size

β, β_0, α and γ also can be organized based on parametric investigations.

The concept of this algorithm is based on the I as the objective function in such way that a firefly is attracted by the brighter one (new solution). As a result of moving toward each other, the distance between the fireflies is updated. Accordingly, the position of the moved firefly after t iteration and implemented update step size of $(x_j - x_i)$ reflects a new solution (x_i^{new}) that further should be evaluated by the fitness function (FT) in the population by:

$$x_i^{new} = x_i^t + \beta_0 e^{-\gamma r_{ij}^2} (x_j - x_i) + \alpha (rand - 0.5) \quad (7)$$

where i, j denotes the index of fireflies and the $rand$ function corresponds a random number of solutions. Using this iterative process only one solution with the lowest FT will be kept [91]. Therefore, each new generated solution, x_i^{new} showing the updated location of firefly is governed by α and γ . Accordingly, the smaller γ , the faster convergence history but the greater β between fireflies. On the other hand, the larger α connote to increasing the range of random motion of fireflies and thereby the slower convergence. In the modified version presented by [69], Equation (7) was updated through the brightness expectation value, using:

$$x_i^{modified} = x_i + \beta_0 e^{-\gamma r_{ij}^2} (x_j - x_i) + \alpha_t r_{ij} (rand - 0.5) \quad (8)$$

Accordingly, α and γ then adaptively are tuned and updated using the variance of the population of brightness ($Var(I)$) by:

$$\begin{cases} \gamma_t = \gamma_0 + e^{-k \cdot Var(I)} (\gamma_u - \gamma_0) \\ \alpha_t = \alpha_0 - e^{-k \cdot Var(I)} |\alpha_u - \alpha_0| \\ \alpha_0 > \alpha_u, \gamma_u > \gamma_0, k > 0 \end{cases} \quad (9)$$

where, subscripts 0 and u denotes the initial and ultimate values. Using this modification, the convergence speed and the computational time are boosted and strengthened [69].

3. Developing Hybrid Adaptive Procedure

The hybridizing procedure benefits from integration of different predictive AI model with optimization methods to capture more accurate output and thus higher performance. Therefore, adopting appropriate procedure to apprehend an optimum multitask topology for predictive unit is critical to avoid from over-fitting problem, early convergence and not getting stuck in local minima. Figure 3 depicts the block-based hybrid adaptive *DNLS-MFA* procedure subjected to iterative constructive technique that using several inner nested loops was programmed in C++. In this approach, 80% of randomized data is used for training. Through the adopted k-fold checking (here set for 10 times), the data then internally are re-randomized into 60% and 20% for training and testing. The remained 20% of unseen data was used for model validation. This iterate-based adaptive procedure was configured for leading to an optimum multitask *DNLS* with a proper adjustment of the internal characteristics and corresponding hyper parameters. To reduce the computational time, the number of maximum hidden layers and used neurons were limited to 3 and 30, respectively. The learning rate also was managed within [0.001, 1.000] interval with a step size of 0.05. The first priority to terminate the training process is to achieve the minimum network root mean square error (*RMSE*) and if not satisfied then the number of iterations (t) will active as set for 500 in this study.

Figure 4a shows the results of series dynamically monitored and analyzed architectures depend upon the implemented training algorithm (*TA*), learning rate and activation function (*AF*). According to Figure 4b, the *DNLS* topology with structure of 4-15-5-2 trained by limited memory quasi-Newton (*LMQN*) subjected to hyperbolic tangent (*Hyft*) activation function can be selected as optimal. In the given topology, 4 denotes the number of used inputs (X, Y, Z, Ts), 15 and 5 express the number of managed neurons in first and second hidden layers and 2 is assigned to the multiple outputs comprising the temperature at depths 50, 150 m ($T50, T150$), respectively.

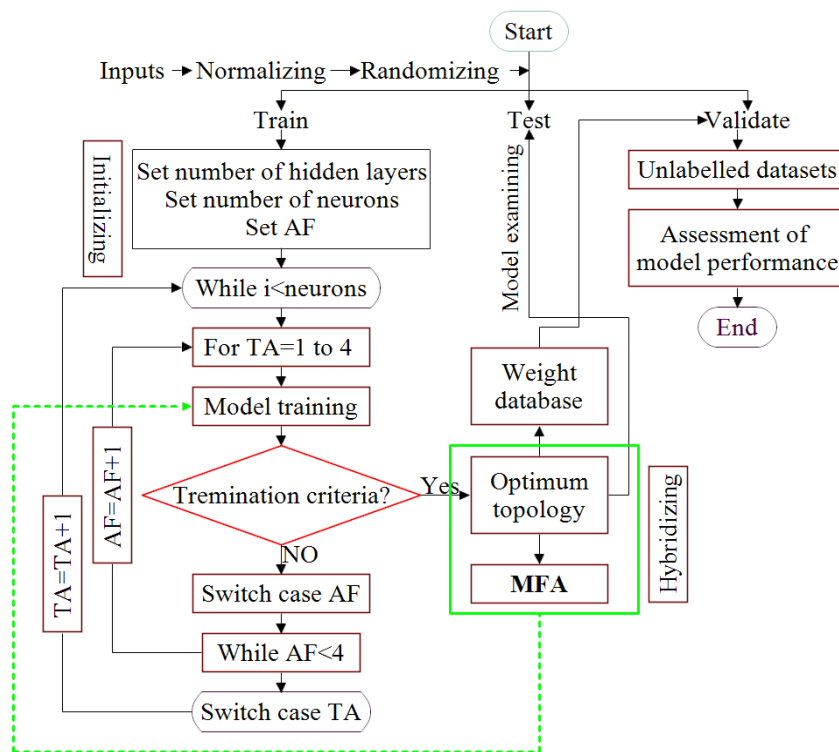


Figure 3. Block diagram of developed adaptive hybridized multitask learning procedure to capture the optimum topology.

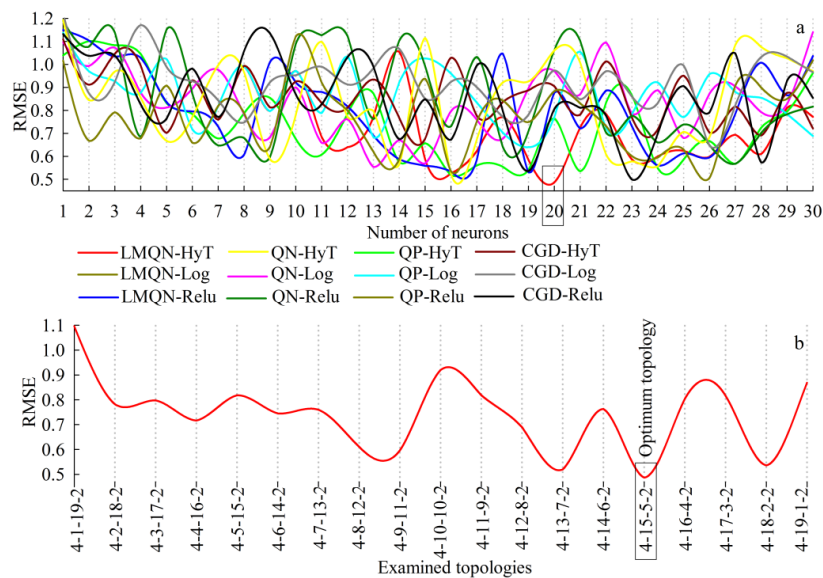


Figure 4. Performance of series monitored topologies as a function of *RMSE* subjected to different *TA* and *AF* (a), and examined topologies to find the optimum model corresponding to 20 neurons (b) (*TA*→*LMQN*: limited memory quasi-Newton, *CGD*: conjugate gradient descent, *QN*: quasi-Newton, *QP*: quick propagation; *AF*→*Log*: logistic, *HyT*: hyperbolic tangent, *Relu*: rectified linear unit).

As presented in Figure 3, the selected optimum topology (Figure 4b) is hybridized with the *MFA*. Referring to Table 1 and Equations (7)–(9), the updated location of firefly should be tuned using α , β and γ . However, appropriate setting of these parameters is not easy task. The most representative values of α , β and γ then were captured through parametric regularizing procedure. Figure 5a shows the result of a series of analyses subjected to *RMSE* with two fixed parameters and one variable. The results showed that the values

of 1, 0.5, 0.2, 0.5 corresponding to γ , β , α , β_0 (Figure 5a) and 30 for population of fireflies (Figure 5b) can be the optimal. Accordingly, the predictability of the model using adaptive *DNLS* (Figure 5c,d) and the hybrid *DNLS-MFA* (Figure 5e,f) were presented and compared.

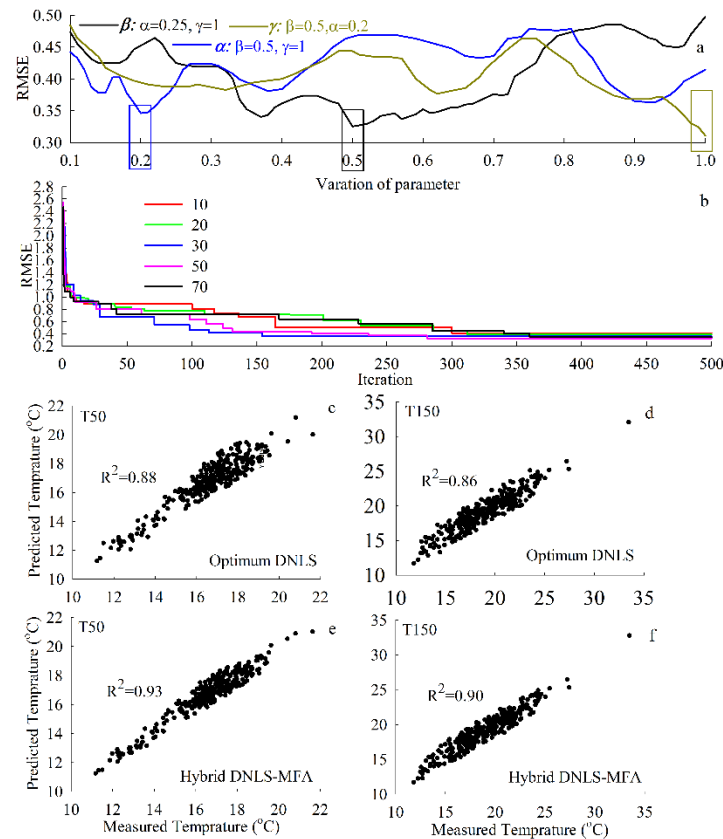


Figure 5. Adjusting the optimal values of *MAF* parameters (a), selected population of fireflies using convergence histories (b), and compared predictability of the optimum and hybrid *DNLS* model (c–f).

Traditional 3D modelling techniques are subjective and limited to the knowledge and experiences of experts in the selection of assumptions and parameters. For subsurface geothermal purposes, therefore, creating 3D depth-dependent digitized spatial predictive maps using identified hybrid optimum *DNLS* model play an important priority. As a result, for the study area, the created 3D maps using the hybrid *DNLS-MFA* at the surface and depth of 50 and 150 m are presented (Figure 6a–c). The applicability of the *DNLS-MFA* then was examined using unlabelled data for two other depths. Accordingly, the elevation was replaced by converted depths for 120 and 180 m with respect to the ground surface elevation with the same used input data. The model then was trained for the whole datasets through the saved weight database and the visualized results were reflected in Figure 6d,e. According to the documented results by Colmenar-Santos et al. (2016) [92] from the report of Institute for the Diversification and Saving of Energy (IDEA), the range of predicted subsurface temperatures show appropriate compatibilities. The predicted subsurface temperature using the applied model at depth of 150 m dedicated about 33 °C, where considering the nonlinearity and heterogeneity it is expected to fall around 70 at 300 m depth. Therefore, referring to [92], the subsurface temperature in the study area corresponding to the depths between 300–2500 m will fall within the interval of [70 °C, 140 °C].

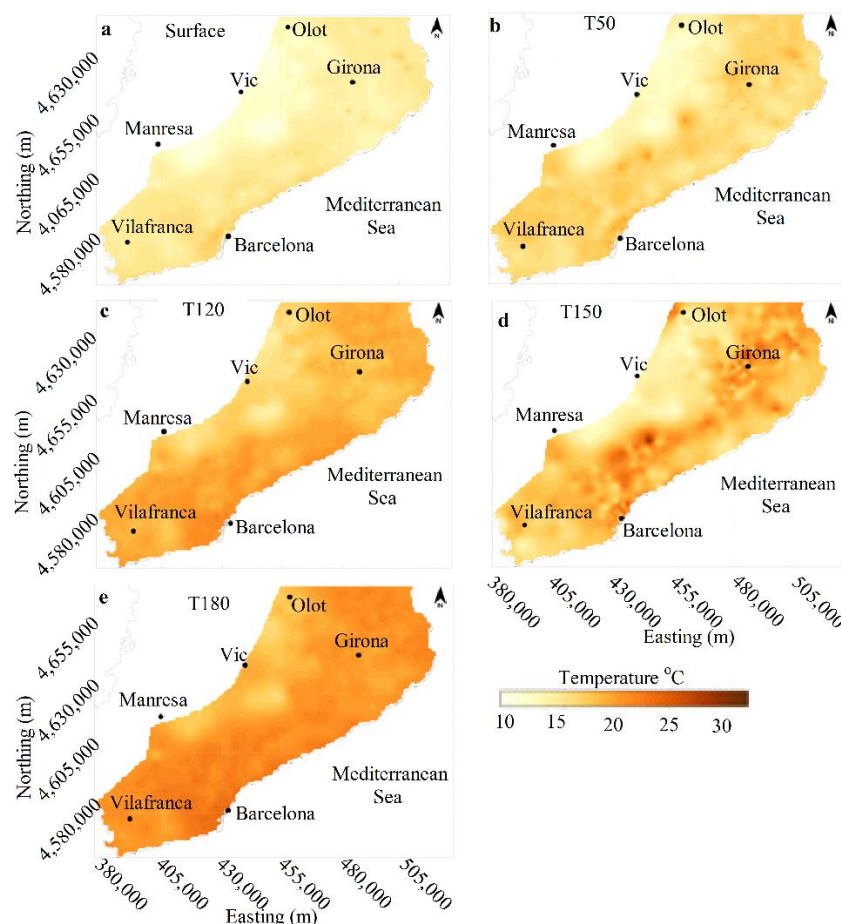


Figure 6. The spatial distribution of surface temperature (a) and corresponding 3D predictive map of the study area using hybrid *DNLS-MFA* model at the depths 50 m (b), 120 m (c), 150 m (d) and 180 m (e).

4. Discussion and Validation

Generally, the statistical error metrics are used to evaluate the performance of the complex models through pair-wise-matched of observations and predictions [93]. In this study, as presented in Table 2 the models were assessed by means of the mean absolute percentage error (*MAPE*), *RMSE*, index of agreement (*IA*) [94] and R^2 . The better performance was selected by higher *IA*, R^2 accompanying with lower *MAPE* and *RMSE*. Table 2 reflects the comparison of the applied metrics for the 15% of unseen randomized validation datasets through the weight database.

Table 2. Evaluated error metrics of the predicted temperatures using validation datasets.

	Optimum <i>DNLS</i>		Hybrid <i>DNLS-MFA</i>	
	<i>T50</i>	<i>T150</i>	<i>T50</i>	<i>T150</i>
R^2	0.87	0.86	0.92	0.91
<i>RMSE</i>	0.49	1.00	0.37	0.79
<i>MAPE</i>	2.40	4.00	1.80	3.2
<i>IA</i>	0.96	0.96	0.98	0.97

Using confusion matrix [95], the predictability performance of developed models is analyzed, where each diagonal entry of $[a_{ij}]$ as the number of records for *i*th and *j*th category of target and corresponding network output would be non-zero. In this study, the multiclass confusion matrixes for optimum and hybridized *DNLS* models using validation datasets were established (Table 3). The cells with value of 0 shows there is no predicted

result correspond to target output. This can be an indicator of appropriate predictability of developed models. Accordingly, the compared qualitative characteristics in classification tasks using correct classification rate (CCR) (Table 4) showed at least 4.2% improvement in the predictability level of hybrid *DNLS* than the optimum topology.

Table 3. Confusion matrix of optimum models using validation datasets.

Target Output	Output of Optimum <i>DNLS</i> : 50 m Depth											Results			
	<12.01	12.01–12.69	12.69–13.38	13.38–14.06	14.06–14.75	14.75–15.43	15.43–16.11	16.11–16.80	16.80–17.48	17.48–18.17	18.17–18.85	>18.85	Total	True	False
12.01–12.69		2		1									3	2	1
12.69–13.38			0										0	0	0
13.38–14.06				1									1	1	0
14.06–14.75					1								1	1	0
14.75–15.43						2							3	2	1
15.43–16.11							1						10	7	3
16.11–16.80								7					16	16	2
16.80–17.48									1				18	18	3
17.48–18.17										2			10	8	2
18.17–18.85											1		7	5	2
Note	0	2	0	2	1	3	8	18	20	12	6	1	74	60	14

Target Output	Output of Hybrid <i>DNLS</i> : 50 m Depth											Results			
	<12.01	12.01–12.69	12.69–13.38	13.38–14.06	14.06–14.75	14.75–15.43	15.43–16.11	16.11–16.80	16.80–17.48	17.48–18.17	18.17–18.85	>18.85	Total	True	False
12.01–12.69		2		1									3	2	1
12.69–13.38			0										0	0	0
13.38–14.06				1									1	1	0
14.06–14.75					0								1	0	1
14.75–15.43						3							3	3	0
15.43–16.11							1						10	8	2
16.11–16.80								8					17	17	1
16.80–17.48									1				20	20	1
17.48–18.17										1			10	8	2
18.17–18.85											1		7	6	1
Note	0	2	1	1	0	5	9	17	22	9	7	1	74	65	9

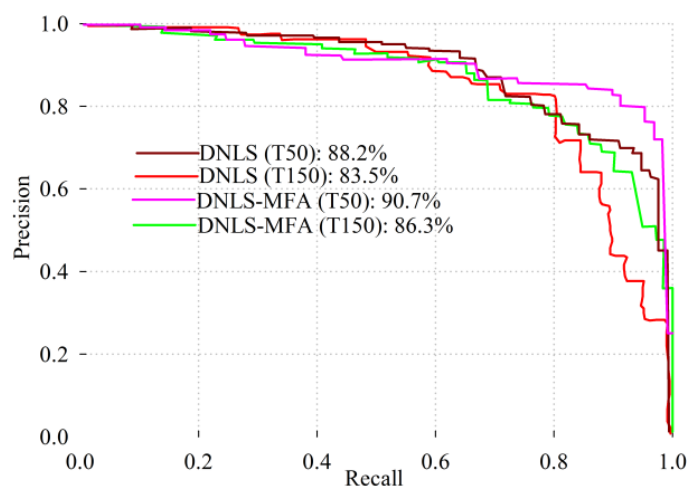
Target Output	Output of Optimum <i>DNLS</i> : 150 m Depth											Results			
	<13.66	13.66–14.73	14.73–15.8	15.8–16.87	16.87–17.94	17.94–19.01	19.01–20.08	20.08–21.15	21.15–22.22	22.22–23.29	23.29–24.36	>24.36	Total	True	False
13.66–14.73	1	1	1										3	1	2
14.73–15.8			3	1									4	3	1
15.8–16.87				4		1							6	4	2
16.87–17.94					4		1						5	4	1
17.94–19.01						8		1					10	8	2
19.01–20.08							1	10					13	10	3
20.08–21.15									1				12	10	2
21.15–22.22										8			9	8	1
22.22–23.29											5		7	5	2
23.29–24.36												4	5	4	1
Note	1	1	5	5	6	10	13	13	7	7	5	1	74	57	17

Target Output	Output of Hybrid <i>DNLS</i> : 150 m depth											Results			
	<13.66	13.66–14.73	14.73–15.8	15.8–16.87	16.87–17.94	17.94–19.01	19.01–20.08	20.08–21.15	21.15–22.22	22.22–23.29	23.29–24.36	>24.36	Total	True	False
13.66–14.73	1	2											3	2	1
14.73–15.8			3	1									4	3	1
15.8–16.87				4									6	4	2
16.87–17.94					4								5	4	1
17.94–19.01						9		1					10	9	1
19.01–20.08							1	11					13	11	2
20.08–21.15									1				12	11	1
21.15–22.22										8			9	8	1
22.22–23.29											5		7	5	2
23.29–24.36												3	5	3	2
Note	1	2	4	5	6	10	12	13	9	6	4	2	74	60	14

Table 4. Comparing the CCR and model improvement using validation data.

Model	CCR (%)	Improved Progress
Optimum DNLS-T50	81.1	6.24%
Hybrid DNLS-T50	86.5	
Optimum DNLS-T150	77.1	4.93%
Hybrid DNLS-T150	81.1	

The presented confusion matrix (Table 3) then was used to plot the area under the curve of receiver operating characteristics (AUC_{ROC}). The ROC is a 2D graphical probability approach to assess the overall performance of a model, where the greater AUC the higher capability in diagnosed classes [96,97]. Precision shows the true predictions in each class and recall reflects the ability of model in identifying the actual positives. Therefore, the predictability of a model in a full picture at different thresholds can be quantified using the precision–recall ROC curves. Referring to Figure 7, the achieved accuracies of 90.7% and 86.3% using hybrid DNLS-MFA for T50 and T150 demonstrated more reliable outputs than optimum DNLS.

**Figure 7.** Comparing the predictability level of optimum multitask and hybrid DNLS models using the AUC_{ROC} of conducted precision–recall curves.

In computational systems the uncertainty analysis for the new individual upcoming observations can be estimated using prediction interval (PI) [98]. One of the key benefits of PI is referred to dedicating a range of weights allowing for insight into how accurate the predicted weight is likely to be [99]. The PI is always wider than a confidence interval because it considers the uncertainty in both predicting the population mean and the random variation of the individual values [100]. In this study, the PI of the hybrid DNLS-MFA at the level of 95% was estimated using a state-of-the-art automated random deactivating weight approach [101], as shown in Figure 8. The applied approach [101] subjected to hybrid DNLS-MFA for T50 and T150 showed narrower distribution of PI , leading to the identification of the potential hot spot sub-areas with lower uncertainty.

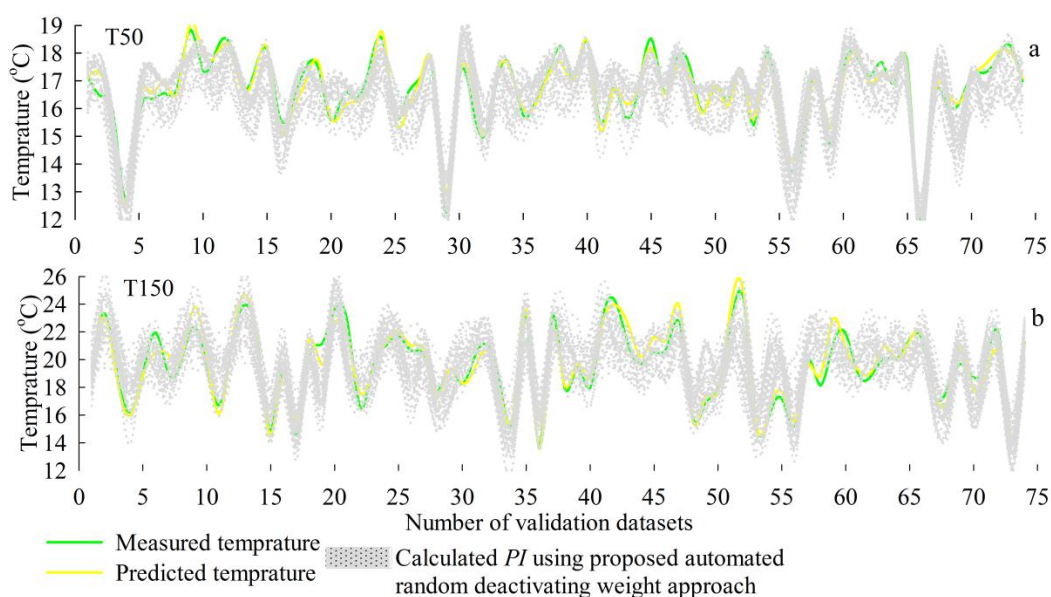


Figure 8. Analyzed uncertainty of hybrid *DNSL-MFA* for *T50* (a) and *T150* (b) using automated random deactivating weight approach according to Ref. [101].

5. Conclusions

Mapping the subsurface temperature in complex structural settings using advanced *DNLS* can dedicate a viable tool for exploration analyses and thus drilling phases. Refer to this motivation, an adaptive hybrid multitask *DNLS-MFA* procedure for producing the 3D predictive spatial maps of the temperature-at-depths was developed and applied on 494 geo-location and surface temperature datasets in a part of Catalonia, Spain. Compared with *DNLS*, the predicted maps at depths of 50 and 150 m using the introduced hybrid *DNLS-MFA* scheme showed 90.7% and 86.3% accuracy performances leading to 6.24% and 4.93% improvements, respectively. The evaluations then were supplemented by error criteria and uncertainty analysis, where the narrower distribution of *PI* in hybrid *DNLS-MFA* showed higher reliability in identifying the most compatible potentials in the study area. Accordingly, the predictability of the hybrid model was then examined with unlabelled data at depths 120 and 180 m, in which the created 3D maps showed appropriate responses to categorized subsurface temperatures. Using the generated 3D visualized maps not only the spatial extension of the interested areas at investigated depth are recognized but also facilitate the interpretability of subsurface heating conditions and, consequently, reducing the geothermal exploration costs. This implies on applicability of produced maps in reflecting the most favorable hotspot locations for further geothermal analyses and thus better site characterizing for field and real-world applications. The presented hybrid *DNLS-MFA* is preferred because the produced digitized 3D spatial maps can be updated using new geoscientific data to improve serving for deeper insights into the geothermal resource systems. However, more knowledge on potential subsurface hot spots is needed to enhance geothermal energy use and public awareness.

Author Contributions: Conceptualization, S.P.M.L., D.P. and M.H.; methodology, S.P.M.L. and A.A.S.; code development and visualization, S.P.M.L. and A.A.S.; validation, S.P.M.L. and A.A.S.; formal analysis, S.P.M.L., D.P., M.H. and A.A.S.; data curation, S.P.M.L.; writing—original draft preparation, S.P.M.L.; writing—review by A.A.S., D.P. and M.H.; thoroughly was edited by native expert. All authors have read and agreed to the published version of the manuscript.

Funding: This research received no external funding.

Institutional Review Board Statement: Not applicable.

Informed Consent Statement: Not applicable.

Data Availability Statement: Not applicable.

Conflicts of Interest: The authors declare no conflict of interest. There is no funder role in the design of the study; in the collection, analyses, or interpretation of data; in the writing of the manuscript; or in the decision to publish the results.

References

1. Lund, J.W. Characteristics, development and utilization of geothermal resources. *Geo-Heat Cent. Q. Bull. Klamath Falls Inst. Technol.* **2007**, *28*, 140–147.
2. Tester, J.W.; Anderson, B.J.; Batchelor, B.J.; Blackwell, D.D.; DiPippo, R.; Drake, E.M.; Garnish, J.; Livesay, B.; Moore, M.C.; Nichols, K.; et al. The Future of Geothermal Energy. In *Impact of Enhanced Geothermal Systems (EGS) on the United States in the 21st Century*; Renewable Energy and Power Department, Idaho National Laboratory: Idaho Falls, ID, USA, 2006. Available online: <http://geothermal.inel.gov> (accessed on 24 May 2022).
3. McLarty, L.; Reed, M.J. The US geothermal industry: Three decades of growth. *Energy Sources* **1992**, *14*, 443–455. [[CrossRef](#)]
4. Lesmana, A.; Winofa, N.C.; Pratama, H.B.; Ashat, A.; Saptadji, N.M. Preliminary financial modelling with probabilistic approach for geothermal development project in Indonesia. *IOP Conf. Ser. Earth Environ. Sci.* **2020**, *417*, 012024. [[CrossRef](#)]
5. Antics, M.; Sanner, B. Status of geothermal energy use and resources in Europe. In Proceedings of the European Geothermal Congress, Unterhaching, Germany, 30 May–1 June 2007.
6. Lund, J.W.; Toth, A.N. Direct utilization of geothermal energy 2020 worldwide review. In Proceedings of the World Geothermal Congress, Reykjavik, Iceland, 24–27 October 2021.
7. Chamorro, C.R.; Garcia-Cuesta, J.L.; Modejar, M.E.; Linares, M.M. An estimation of the enhanced geothermal system potential for the Iberian Peninsula. *Renew. Energy* **2014**, *66*, 1–14. [[CrossRef](#)]
8. Sanchez-Guzman, J.; García de la Noceda, C. The evolution of geothermal energy in Spain-country update (2005–2009). In Proceedings of the World Geothermal Congress, Bali, Indonesia, 25–29 April 2010.
9. Arrizabalaga, I.; De Gregorio, M.; De Santiago, C.; García de la Noceda, C.; Pérez, P.; Urchueguía, J.F. Geothermal energy use, country update for Spain. In Proceedings of the European Geothermal Congress, Den Haag, The Netherlands, 11–14 June 2019.
10. Hochstein, M.P.; Brown, P.R.L. Surface manifestations of geothermal systems with volcanic heat sources. In *Encyclopedia of Volcanoes*; Sigurdsson, H., Ed.; Academic Press: San Diego, CA, USA, 2000; pp. 835–855.
11. Montanari, D.; Lupi, M.; Calcagno, P. Geothermal systems: Interdisciplinary approach for an effective exploration. *Geofluids* **2019**, *2019*, 9895659. [[CrossRef](#)]
12. Omodeo-Salé, S.; Eruteya, O.E.; Cassola, T.; Baniasad, A.; Moscariello, A. A basin thermal modelling approach to mitigate geothermal energy exploration risks: The St. Gallen case study (eastern Switzerland). *Geothermics* **2020**, *87*, 101876. [[CrossRef](#)]
13. Matsumoto, M. An approach for estimating geothermal reservoir productivity under access limitations associated with snowy and mountainous prospects. In *Geothermal Energy*; Ismail, B.I., Ed.; IntechOpen Press: London, UK, 2021. [[CrossRef](#)]
14. Hochstein, M.P. Assessment and modelling of geothermal reservoirs (small utilization schemes). *Geothermics* **1998**, *17*, 15–49. [[CrossRef](#)]
15. Ilyasov, M.; Ostermann, I.; Punzi, A. Modeling Deep Geothermal Reservoirs: Recent Advances and Future Problems. In *Handbook of Geomathematics*; Freedon, W., Nashed, M.Z., Sonar, T., Eds.; Springer: Berlin/Heidelberg, Germany, 2010. [[CrossRef](#)]
16. Gumming, W. A conceptual model approach to the geophysical exploration of permeable geothermal reservoirs that considers context and uncertainty. *SEG Tech. Program Expand. Abstr.* **2009**, 4326–4330. [[CrossRef](#)]
17. Gao, J.; Shi, Q. A new mathematical modeling approach for thermal exploration efficiency under different geothermal well layout conditions. *Sci. Rep.* **2021**, *11*, 22930. [[CrossRef](#)]
18. Zhu, Z.; Lei, X.; Xu, N.; Shao, D.; Jiang, X.; Wu, X. Integration of 3D geological modeling and geothermal field analysis for the evaluation of geothermal reserves in the northwest of Beijing Plain, China. *Water* **2020**, *12*, 638. [[CrossRef](#)]
19. Fulignati, P.; Marianelli, P.; Sbrana, A.; Ciani, V. 3D geothermal modelling of the Mount Amiata Hydrothermal system in Italy. *Energies* **2014**, *7*, 7434–7453. [[CrossRef](#)]
20. Noorollahi, Y.; Itoi, R.; Fujii, H.; Tanaka, T. GIS model for geothermal resource exploration in Akita and Iwate prefectures, northern Japan. *Comput. Geosci.* **2007**, *33*, 1008–1021. [[CrossRef](#)]
21. Schiel, K.; Baume, O.; Caruso, G.; Leopold, U. GIS-based modelling of shallow geothermal energy potential for CO₂ emission mitigation in urban areas. *Renew. Energy* **2016**, *86*, 1023–1036. [[CrossRef](#)]
22. Meng, F.; Liang, X.; Xiao, C.; Wang, G. Geothermal resource potential assessment utilizing GIS-based multi criteria decision analysis method. *Geothermics* **2021**, *89*, 101969. [[CrossRef](#)]
23. Tende, A.W.; Aminu, M.D.; Gajere, J.N. A spatial analysis for geothermal energy exploration using bivariate predictive modelling. *Scientific Rep.* **2021**, *11*, 19755. [[CrossRef](#)]
24. Moghaddam, M.K.; Noorollahi, Y.; Samadzadegan, F.; Sharifi, M.A.; Itoi, R. Spatial data analysis for exploration of regional scale geothermal resources. *J. Volcanol. Geotherm. Res.* **2013**, *266*, 69–83. [[CrossRef](#)]
25. Carranza, E.J.M.; Wibowo, H.; Barritt, S.D.; Sumintadireja, P. Spatial data analysis and integration for regional-scale geothermal potential mapping, West Java, Indonesia. *Geothermics* **2008**, *37*, 267–299. [[CrossRef](#)]

26. Makasis, N.; Kreitmair, M.J.; Bidarmaghz, A.; Farr, G.J.; Sceidegger, J.M.; Choudhary, R. Impact of simplifications on numerical modelling of the shallow subsurface at city-scale and implications for shallow geothermal potential. *Sci. Total Environ.* **2021**, *791*, 148236. [[CrossRef](#)]
27. Pola, M.; Fabbri, P.; Piccinini, L.; Zampieri, D. Conceptual and numerical models of a tectonically-controlled geothermal system: A case study of the Euganean Geothermal System, Northern Italy. *Cent. Eur. Geol.* **2015**, *58*, 129–151. [[CrossRef](#)]
28. Arola, T.; Korhonen, K.; Martinkauppi, A.; Leppäharju, N.; Hakala, P.; Ahonen, L.; Pashkovskii, M. Creating shallow geothermal potential maps for Finland. In Proceedings of the European Geothermal Congress, Den Haag, The Netherlands, 11–14 June 2019.
29. Balling, N.; Poulsen, S.E.; Fuchs, S.; Mathiesen, A.; Bording, T.S.; Nielsen, S.B.; Nielsen, L.H. Development of a numerical 3D geothermal model for Denmark. In Proceedings of the European Geothermal Congress, Strasbourg, France, 19–24 September 2016.
30. Yadav, K.; Shah, M.; Sircar, A. Application of magnetotelluric (MT) study for the identification of shallow and deep aquifers in Dholera geothermal region. *Groundw. Sustain. Dev.* **2021**, *11*, 100472. [[CrossRef](#)]
31. Chiang, C.W.; Yang, Z.X.; Chen, C.C.; Yeh, E.C.; Chen, C.S.; Wang, C.Y. Potential geothermal structure inferred from the electrical resistivity and seismic reflection models in the western Ilan Plain, NE Taiwan. *Geothermics* **2021**, *94*, 102124. [[CrossRef](#)]
32. Di Paolo, J.F.; Ledo, J.; Slezak, K.; Van Dorth, D.M.; Pérez, I.C.; Pérez, N. La Palma Island (Spain) geothermal system revealed by 3D magnetotelluric data inversion. *Sci. Rep.* **2020**, *10*, 18181. [[CrossRef](#)] [[PubMed](#)]
33. Mitjanas, G.; Marcuello, A.; Ledo, J.; Macau, A.; Aliás, G.; Queralt, P.; Bellmunt, F.; Rivero, L.I.; Gabas, A.; Benjumea, B.; et al. Integrated seismic ambient noise, magnetotellurics and gravity data for the 2D interpretation of the Vall'es basin structure in the geothermal system of La Garriga-Samalus (NE Spain). *Geothermics* **2021**, *93*, 102067. [[CrossRef](#)]
34. Amatyakul, P.; Prommakorn, N.; Wood, S.H.; Arunwan, T.R.; Vachiratienchai, C.; Chanapiwat, P.; Siripunvaraporn, W. An assessment of a shallow geothermal reservoir of Mae Chan hot spring, northern Thailand via magnetotelluric surveys. *Geothermics* **2021**, *95*, 102137. [[CrossRef](#)]
35. Zaher, M.A.; Saibi, H.; Mansour, K.; Khalil, A.; Soliman, M. Geothermal exploration using airborne gravity and magnetic data at Siwa Oasis, Western Desert, Egypt. *Renew. Sustain. Energy Rev.* **2018**, *82*, 3824–3832. [[CrossRef](#)]
36. Manzella, A.; Viezzoli, A.; Menghini, A.; Santilano, A.; Donato, A.; Montanari, D.; Maggi, S.; Rizzo, E. Shallow geothermal exploration using SkyTEM data: The VIGOR experiment. In Proceedings of the European Geothermal Congress EGC, Pisa, Italy, 3–7 June 2013.
37. Nieto, I.M.; Martín, A.F.; García, P.C.; Blázquez, C.S.; Aguilera, D.G.; García, J.C. Geophysical Prospecting for Geothermal Resources in the South of the Duero Basin (Spain). *Energies* **2020**, *13*, 5397. [[CrossRef](#)]
38. Navarro, A.; Carulla, N. Evaluation of geothermal potential in the vicinity of the flooded Sierra Almagrera Mines (Almeria, SE Spain). *Mine Water Environ.* **2018**, *37*, 137–150. [[CrossRef](#)]
39. Daniele, L.; Taucare, M.; Viguier, B.; Arancibia, G.; Aravena, D.; Roquer, T.; Sepúlveda, J.; Molina, E.; Delgado, A.; Muñoz, M.; et al. Exploring the shallow geothermal resources in the Chilean Southern Volcanic Zone: Insight from the Liquiñe thermal springs. *J. Geochem. Explor.* **2020**, *218*, 106611. [[CrossRef](#)]
40. Mallet, J.L. Discrete smooth interpolation in geometric modeling. *Comp. Comput.-Aided Des.* **1992**, *24*, 178–191. [[CrossRef](#)]
41. Zhu, J.; Wright, G.; Wang, J.; Wang, X. A critical review of the integration of geographic information system and building information modelling at the data level. *ISPRS Int. J. Geo-Inf.* **2018**, *7*, 66. [[CrossRef](#)]
42. Choi, Y.; Baek, J.; Park, S. Review of GIS-based applications for mining: Planning, operation, and environmental management. *Appl. Sci.* **2020**, *10*, 2266. [[CrossRef](#)]
43. Chen, X.W.; Lin, X. Big data deep learning: Challenges and perspectives. *IEEE Access* **2014**, *2*, 514–525. [[CrossRef](#)]
44. Karpatne, A.; Ebert-Uphoff, I.; Ravela, S.; Babaie, H.A.; Kumar, V. Machine learning for the geosciences: Challenges and opportunities. *IEEE Trans. Knowl. Data Eng.* **2018**, *31*, 1544–1554. [[CrossRef](#)]
45. Spina, R. Big data and artificial intelligence analytics in geosciences: Promises and potential. GSA Today Archive. *Geol. Soc. Am.* **2019**, *29*, 42–43. [[CrossRef](#)]
46. Abbaszadeh Shahri, A.; Shan, C.; Zall, E.; Larsson, S. Spatial distribution modeling of subsurface bedrock using a developed automated intelligence deep learning procedure: A case study in Sweden. *J. Rock Mech. Geotech. Eng.* **2021**, *13*, 1300–1310. [[CrossRef](#)]
47. Ghaderi, A.; Abbaszadeh Shahri, A.; Larsson, S. An artificial neural network-based model to predict spatial soil type distribution using piezocone penetration test data (CPTu). *Bull. Eng. Geol. Environ.* **2019**, *78*, 4579–4588. [[CrossRef](#)]
48. Abbaszadeh Shahri, A.; Larsson, S.; Renkel, C. Artificial intelligence models to generate visualized bedrock level: A case study in Sweden. *Modeling Earth Syst. Environ.* **2020**, *6*, 1509–1528. [[CrossRef](#)]
49. Abbaszadeh Shahri, A.; Kheiri, A.; Hamzeh, A. Subsurface topographic modeling using geospatial and data driven algorithm. *ISPRS Int. J. Geo-Inf.* **2021**, *10*, 341. [[CrossRef](#)]
50. Nguyen, X.C.; Nguyen, T.T.H.; Le, Q.V.; Le, P.C.; Srivastav, A.L.; Pham, Q.B.; Nguyen, P.M.; La, D.D.; Rene, E.R.; Ngo, H.H.; et al. Developing a new approach for design support of subsurface constructed wetland using machine learning algorithms. *J. Environ. Manag.* **2022**, *301*, 113868. [[CrossRef](#)]
51. Li, H.; Misra, S. Robust machine-learning workflow for subsurface geomechanical characterization and comparison against popular empirical correlations. *Expert Syst. Appl.* **2021**, *177*, 114942. [[CrossRef](#)]
52. Schmidhuber, J. Deep learning in neural networks: An overview. *Neural Netw.* **2015**, *61*, 85–117. [[CrossRef](#)] [[PubMed](#)]

53. Harp, D.R.; O'Malley, D.; Yan, B.; Pawar, R. On the feasibility of using physics-informed machine learning for underground reservoir pressure management. *Expert Syst. Appl.* **2021**, *178*, 115006. [[CrossRef](#)]
54. Chen, Y.; Zhang, D. Physics-constrained deep learning of geomechanical logs. *IEEE Trans. Geosci. Remote Sens.* **2020**, *58*, 5932–5943. [[CrossRef](#)]
55. Duplyakin, D.; Beckers, K.; Siler, D.; Martin, M.J.; Johnston, H. Modeling subsurface performance of a geothermal reservoir using machine learning. *Energies* **2022**, *15*, 967. [[CrossRef](#)]
56. Witter, J.B.; Trainor-Guitton, W.J.; Siler, D.L. Uncertainty and risk evaluation during the exploration stage of geothermal development: A review. *Geothermics* **2019**, *78*, 233–242. [[CrossRef](#)]
57. Singh, U.K.; Tiwarib, R.K.; Singh, S.B. Neural network modeling and prediction of resistivity structures using VES Schlumberger data over a geothermal area. *Comput. Geosci.* **2013**, *52*, 246–257. [[CrossRef](#)]
58. Yadav, A.; Yadav, K.; Sircar, A. Feedforward neural network for joint inversion of geophysical data to identify geothermal sweet spots in Gandhar, Gujarat, India. *Energy Geosci.* **2021**, *2*, 189–200. [[CrossRef](#)]
59. Gudmundsdottir, H.; Horne, R.N. Prediction modeling for geothermal reservoirs using deep learning. In Proceedings of the 45th Workshop on Geothermal Reservoir Engineering, SGP-TR-216, Stanford, CA, USA, 10–12 February 2020.
60. Kaftana, I.; Salka, M.; Senolb, Y. Evaluation of gravity data by using artificial neural networks case study: Seferihisar geothermal area (Western Turkey). *J. Appl. Geophys.* **2011**, *75*, 711–718. [[CrossRef](#)]
61. Spichak, V. Estimating temperature distributions in geothermal areas using a neuronet approach. *Geothermics* **2006**, *35*, 181–197. [[CrossRef](#)]
62. Shahdi, A.; Lee, S.; Karpatne, A.; Nojabaei, B. Exploratory analysis of machine learning methods in predicting subsurface temperature and geothermal gradient of Northeastern United States. *Geotherm. Energy* **2021**, *9*, 18. [[CrossRef](#)]
63. Siler, D.L.; Pepin, J.D.; Vesselinov, V.V.; Mudunuru, M.K.; Ahmed, B. Machine learning to identify geologic factors associated with production in geothermal fields: A case-study using 3D geologic data, Brady geothermal field, Nevada. *Geotherm. Energy* **2021**, *9*, 17. [[CrossRef](#)]
64. Bourhis, P.; Cousin, B.; Loria, A.F.R.; Laloui, L. Machine learning enhancement of thermal response tests for geothermal potential evaluations at site and regional scales. *Geothermics* **2021**, *95*, 102132. [[CrossRef](#)]
65. Yang, X.S. Metaheuristic optimization: Algorithm analysis and open problems. In *Experimental Algorithms, SEA*; Pardalos, P.M., Rebennack, S., Eds.; Lecture Notes in Computer Science; Springer: Berlin/Heidelberg, Germany, 2011; Volume 6630. [[CrossRef](#)]
66. Mansouri, A.; Aminnejad, B.; Ahmadi, H. Introducing modified version of penguins search optimization algorithm (PeSOA) and its application in optimal operation of reservoir systems. *Water Supply* **2018**, *18*, 1484–1496. [[CrossRef](#)]
67. Asheghi, R.; Abbaszadeh Shahri, A.; Khorsand Zak, M. Prediction of uniaxial compressive strength of different quarried rocks using metaheuristic algorithm. *Arab. J. Sci. Eng.* **2019**, *44*, 8645–8659. [[CrossRef](#)]
68. Oliveira, P.M.; Pires, E.J.S.; Boaventura-Cunha, J.; Pinho, T.M. Review of nature and biologically inspired metaheuristics for greenhouse environment control. *Trans. Inst. Meas. Control* **2020**, *42*, 2338–2358. [[CrossRef](#)]
69. Abbaszadeh Shahri, A.; Khorsand Zak, M.; Abbaszadeh Shahri, H. A modified firefly algorithm applying on multi-objective radial-based function for blasting. *Neural Comput. Appl.* **2022**, *34*, 2455–2471. [[CrossRef](#)]
70. Shi, Y.; Eberhart, R. A modified particle swarm optimizer. In Proceedings of the IEEE, International Conference on Evolutionary Computation Proceedings, IEEE World Congress on Computational Intelligence (Cat. No. 98TH8360), Anchorage, AK, USA, 4–9 May 1998. [[CrossRef](#)]
71. Faritha, B.A.; Chandrasekar, C. An optimized approach of modified bat algorithm to record deduplication. *Int. J. Comput. Appl.* **2013**, *62*, 10–15. [[CrossRef](#)]
72. Yang, X.S. *Nature-Inspired Metaheuristic Algorithms*; Luniver Press: Cambridge, UK, 2008.
73. Chou, J.S.; Ngo, N.T. Modified firefly algorithm for multidimensional optimization in structural design problems. *Struct. Multidiscip. Optim.* **2017**, *55*, 2013–2028. [[CrossRef](#)]
74. Blázquez, C.S.; Maté-González, M.A.; Nieto, I.M.; Martín, A.F.; González-Aguilera, D. Assessment of the geothermal potential in the region of Ávila (Spain): An integrated and interactive thermal approach. *Geothermics* **2022**, *98*, 102294. [[CrossRef](#)]
75. PANER. *Plan de Acción Nacional de Energías Renovables de España (2011–2020)*; Spanish Department of Industry Tourism and Commerce: Madrid, Spain, 2010.
76. Ryan, G.A.; Peacock, J.R.; Shalev, E.; Rugis, J. Montserrat geothermal system: A 3D conceptual model. *Geophys. Res. Lett.* **2013**, *40*, 2038–2043. [[CrossRef](#)]
77. Witter, J.B.; Siler, D.L.; Faulds, J.E.; Hinz, N.H. 3D geophysical inversion modelling of gravity data to test the 3D geologic model of the Bradys geothermal area, Nevada, USA. *Geotherm. Energy* **2016**, *4*, 14. [[CrossRef](#)]
78. Milichich, S.D.; Pearson-Grant, S.C.; Alcaraz, S.; White, P.A.; Tschritter, C. 3D Geological modelling of the Taupo Volcanic Zone as a foundation for a geothermal reservoir model. *N. Z. J. Geol. Geophys.* **2018**, *61*, 79–95. [[CrossRef](#)]
79. Caruana, R. Multitask learning. *Mach. Learn.* **1997**, *28*, 41–75. [[CrossRef](#)]
80. Puigdefàbregas, C.; Muñoz, J.A.; Vergés, J. Thrusting and foreland basin evolution in the southern Pyrenees. In *Thrust Tectonics*; Springer: Dordrecht, The Netherlands, 1992; pp. 247–254. [[CrossRef](#)]
81. Lladó, X.M.; Vilà, M.; Martí, V.; Rovira, M.; Domènech, J.A.; Pablo, J.D. Trace Element Distribution in Topsoils in Catalonia: Background and Reference Values and Relationship with Regional Geology. *Environ. Eng. Sci.* **2008**, *25*, 863–878. [[CrossRef](#)]

82. Bartrina, M.T.; Cabrera, L.; Jurado, M.J.; Guimerà, J.; Roca, E. Evolution of the central Catalan margin of the Valencia trough (western Mediterranean). *Tectonophysics* **1992**, *203*, 219–247. [[CrossRef](#)]
83. Roca, E. The northwest-Mediterranean basin (Valencia Trough, Gulf of Lions and Liguro-Provençal basins): Structure and geo-dynamic evolution. *Mémoires du Muséum Natl. d'Histoire Nat.* **2001**, *168*, 671–706.
84. ICGC Shallow Geothermal Energy. Geoindex (Viewer & Geoservices WMS), February 2021, Institut Cartogràfic i Geològic de Catalunya, Barcelona. Available online: <https://www.icgc.cat/> (accessed on 1 June 2021).
85. ICGC Deep Geothermal Energy. Geoindex (Viewer & Geoservices WMS), October 2020, Institut Cartogràfic i Geològic de Catalunya, Barcelona. Available online: <https://www.icgc.cat/> (accessed on 1 June 2021).
86. Baxter, J. A model of inductive bias learning. *J. Artif. Intell. Res.* **2000**, *12*, 149–198. [[CrossRef](#)]
87. Ando, R.; Zhang, T. A framework for learning predictive structures from multiple tasks and unlabeled data. *J. Mach. Learn. Res.* **2005**, *6*, 1817–1853.
88. Ruder, S. An overview of multi-task learning in deep neural networks. *arXiv* **2017**, arXiv:1706.05098v1.
89. Zhang, Y.; Yang, Q. A survey on multi-task learning. *IEEE Trans. Knowl. Data Eng.* **2021**. [[CrossRef](#)]
90. LeCun, Y.; Bengio, Y.; Hinton, G. Deep learning. *Nature* **2015**, *521*, 436–444. [[CrossRef](#)] [[PubMed](#)]
91. Fister, I.; Yang, X.S.; Brest, J. A comprehensive review of firefly algorithms. *Swarm Evol. Comput.* **2013**, *13*, 34–46. [[CrossRef](#)]
92. Colmenar-Santos, A.; Folch-Calvo, M.; Rosales-Asensio, E.; Borge-Diez, D. The geothermal potential in Spain. *Renew. Sustain. Energy Rev.* **2016**, *56*, 865–886. [[CrossRef](#)]
93. Willmott, C.J. On the validation of models. *Phys. Geogr.* **1981**, *2*, 184–194. [[CrossRef](#)]
94. Willmott, C.J. On the evaluation of model performance in physical geography. *Spat. Stat. Models* **1984**, *40*, 443–460. [[CrossRef](#)]
95. Stehman, S. Selecting and interpreting measures of thematic classification accuracy. *Remote Sens. Environ.* **1997**, *62*, 77–89. [[CrossRef](#)]
96. Bradley, A.P. The use of the area under the ROC curve in the evaluation of machine learning algorithms. *Pattern Recognit.* **1997**, *30*, 1145–1159. [[CrossRef](#)]
97. Fawcett, T. An introduction to ROC analysis. *Pattern Recognit. Lett.* **2006**, *27*, 861–874. [[CrossRef](#)]
98. Meade, N.; Islam, T. Prediction intervals for growth curve forecasts. *J. Forecast.* **1995**, *14*, 413–430. [[CrossRef](#)]
99. Hastie, T.; Tibshirani, R.; Friedman, J. *The Elements of Statistical Learning*, 2nd ed.; Springer: New York, NY, USA, 2001. [[CrossRef](#)]
100. Lawless, J.F.; Fredette, M. Frequentist prediction intervals and predictive distributions. *Biometrika* **2005**, *92*, 529–542. [[CrossRef](#)]
101. Abbaszadeh Shahri, A.; Shan, C.; Larsson, S. A novel approach to uncertainty analysis using automated predictive deep learning in groundwater table modelling. *Nat. Res. Resour.* **2022**, *31*, 1351–1373. [[CrossRef](#)]